PAPER

3D Printing of a Biomimetic Myotendinous Junction Assisted by Artificial Intelligence†

Wisarut Kiratitanaporn, [a] Jiaao Guan,[b] Min Tang,[c] Yi Xiang,[c] Ting-yu Lu,[e] Alis Balayan,[f] Alison Lao, [c] David B. Berry [*c,d] and Shaochen Chen [*a,b,c,e]

The myotendinous junction (MTJ) facilitates force transmission between muscle and tendon to produce joint movement. The complex microarchitecture and regional mechanical heterogeneity of the myotendinous junction pose major challenges in creating this interface *in vitro*. Engineering this junction *in vitro* is challenging due to substantial fabrication difficulties in creating scaffolds with intricate microarchitecture and stiffness heterogeneity to mimic the native muscle–tendon interface. To address the current challenges in creating the MTJ *in vitro*, digital light processing (DLP)-based 3D printing was used to fabricate poly(glycerol sebacate)acrylate (PGSA)-based muscle–tendon scaffolds with physiologically informed microstructure and mechanical properties. Local mechanical properties in various regions of the scaffold were tuned by adjusting the exposure time and light intensity used during the continuous DLP-based 3D printing process to match the mechanical properties present in distinct regions of native muscle–tendon tissue using printing parameters defined by an artificial intelligence-trained algorithm. To evaluate how the presence of zonal stiffness regions can affect the phenotype of a 3D-printed MTJ *in vitro* model, three 3D-printed PGSA-based scaffold conditions were investigated: (1) a scaffold with muscle-informed mechanical properties in its entirety without zonal stiffness regions, (2) a scaffold with one end possessing native muscle stiffness and the other end possessing native tendon stiffness, and (3) a scaffold with three distinct regions whose stiffness values correspond to those of muscle on one end of the scaffold, MTJ in the middle junction of the scaffold, and tendon on the other end of the scaffold. The scaffold containing regional mechanical heterogeneity most similar to the native MTJ (condition 3) was found to enhance the expression of MTJ-related markers compared to those without the presence of zonal stiffness regions. Overall, the DLP-based 3D printing platform and biomaterial system developed in this study could serve as a useful tool for mimicking the complexity of the native MTJ, which possesses inherent geometric and mechanical heterogeneity.

1. Introduction

The musculoskeletal system is crucial for supporting movement from the transmission of force from organized muscle fibers through tendon to bone.[1–4] An interface between skeletal muscle and tendon called the myotendinous junction (MTJ) serves as the main path that allows for efficient force transmission from skeletal muscle to tendon.[4] The MTJ possesses highly interdigitated finger-like projections that serve to reduce stress concentrations at the interface by increasing the surface area at the junction between mechanically distinct tissues (*e.g.* muscle and tendon).[3–7] These structures are preserved across species; there currently is no evidence that relative surface area between species is related to anything other than relative fiber type distribution differences between muscles.[8] The major challenges associated with scaffold-based models of a muscle–tendon junction *in vitro* lie in the complex geometric morphology and heterogeneous mechanical properties that are present in the native muscle–tendon unit.[1–5,9–11]

Developing a biocompatible platform with microarchitecture and three distinct mechanical properties that closely mimic those of native muscle, the MTJ, and tendon within a

[a]*Department of Bioengineering, University of California San Diego, La Jolla, CA, 92093, USA. E-mail: shc064@ucsd.edu*
[b]*Department of Electrical and Computer Engineering, University of California San Diego, La Jolla, CA, 92093, USA*
[c]*Department of NanoEngineering, University of California San Diego, La Jolla, CA, 92093, USA*
[d]*Department of Orthopedic Surgery, University of California San Diego, La Jolla, CA, 92093, USA*
[e]*Materials Science and Engineering Program, University of California San Diego, La Jolla, CA, 92093, USA. E-mail: dbberry@health.ucsd.edu*
[f]*School of Medicine, University of California San Diego, La Jolla, CA, 92093, USA*
†Electronic supplementary information (ESI) available. See DOI: https://doi.org/10.1039/d4bm00892h

single muscle–tendon scaffold presents a significant fabrication challenge.[12] Conventional methods for fabricating tissue-engineered platforms with specific stiffness range and zonal stiffness regions still rely heavily on trial-and-error synthesis that can be economically inefficient in terms of time and resources spent. Furthermore, they often fail to meet the target properties for the intended application.[13] This is further complicated by the biological diversity of the native muscle–tendon unit and the incomplete characterization of the MTJ-related proteome.[14] Rodent muscle–tendon MTJs are frequently studied in place of human MTJs because they are more easily accessible, and share similar material properties, such as the stiffness and tensile strength of muscle and tendon tissues. For example, the stiffness of relaxed muscle tissue is approximately 10 kPa–60 kPa in both humans and rats. Rat tendons are slightly less stiff than human tendons – 300 MPa–900 MPa in rats *vs.* 500 MPa–1500 MPa in humans – however there is still significant overlap in these ranges and rats' tendons are still considered a suitable model.[15,16] These similarities allow researchers to model and investigate key biomechanical behaviors and tissue interactions, while the smaller size and accessibility of rodent models make them more practical for controlled experimental setups. Additionally, rodent models exhibit comparable responses in tissue repair and adaptation to mechanical loading, making them valuable for studying musculoskeletal mechanics and regenerative approaches.

Various fabrication techniques have been employed in previous efforts to model the MTJ. Merceron *et al.* leveraged nozzle-based 3D printing of thermoplastic polyurethane (PU) for muscle and polycaprolactone (PCL) for tendon.[17] Scaffolds were co-printed with a hydrogel-based bioink composed of hyaluronic acid, gelatin, and fibrinogen. C2C12 cells were encapsulated in the bioink for muscle and NIH/3T3 cells were encapsulated for tendon.[17] Despite achieving different spatial mechanical properties, the C2C12 and NIH/3T3 cells were localized to the PU and PCL ends without establishing proper contact at the interface as seen in the native MTJ,[17] and it remains unclear whether the expression of MTJ-related genes was influenced by the cell–bioink interaction or cell–PU/PCL interaction. Extrusion-based 3D printing with a GelMA–PEGMA bioink was also used to print primary tenocytes and myoblasts for a muscle–tendon unit, but weak mechanical integrity of the hydrogel platform resulted in interfacial tearing within 1–2 days.[18] The limitations associated with previous attempts to fabricate muscle–tendon units through nozzle-based 3D printing highlight the need for an alternative microfabrication platform capable of recapitulating native muscle–tendon microarchitecture with high fidelity and structural resolution without nozzle diameter-related limitations. In addition, weak mechanical integrity associated with hydrogel-based bioinks means that a more robust biomaterial system capable of withstanding forces transmitted from skeletal muscle is needed. Josvai *et al.* utilized micropatterning to fabricate MTJ units using human embryonic stem cell-derived myocytes and primary tenocytes.[19] While this system did demonstrate the ability to form a myocyte–tenocyte junction, this approach utilizes a single scaffold stiffness for all regions (10 kPa), and is restricted to a simplified block channel design. Taken together, these challenges underscore the necessity for innovative, new approaches to enhance mimicry of MTJ scaffolds.

Digital light processing (DLP)-based 3D printing technology is a light-based method that can fabricate scaffolds with micron-scale resolution within a few seconds. This continuous 3D printing process photopolymerizes an entire layer of biomaterial at the focal plane, enabling the fabrication of a tissue-engineered scaffold with arbitrarily complex microarchitecture.[20–29] There are two main advantages associated with utilizing DLP-based 3D printing technology for the microfabrication of a muscle–tendon scaffold for *in vitro* mimicry of the MTJ. First, the continuous nature of DLP-based 3D printing allows for the fabrication of scaffolds without structural artificial interfaces,[20,25,30] thus improving the structural and mechanical integrity of 3D-printed structures. Second, DLP-based 3D printing allows for digital modulation of the mechanical properties of the 3D-printed structures through the adjustment of exposure time[25] and light intensity,[31] allowing for a continuous light-based 3D printing of complex scaffolds with arbitrary local stiffness regions.

Engineering musculoskeletal tissues such as the muscle–tendon unit using traditional hydrogel-based scaffold systems presents another challenge, as hydrogels are often too soft to withstand dynamic forces generated by skeletal muscle.[32] Due to this limitation, a more robust biomaterial system capable of withstanding dynamic forces is needed for scaffold-based engineering of muscle–tendon units *in vitro*. Poly(glycerol sebacate)acrylate (PGSA) is a robust, biodegradable elastomer that is highly elastic and biocompatible.[25,33,34] Due to the material's low swelling ratio, PGSA can maintain its structural dimensions without swelling in aqueous microenvironments, as is often seen with hydrogel-based systems.[25,31,33] The photopolymerizable nature of PGSA due to the presence of acrylate functional groups makes it compatible with a DLP-based 3D printing system. In addition, PGSA possesses highly tunable mechanical properties that can be controlled by adjusting the acrylation ratio[33] during the chemical synthesis process or by adjusting the exposure time and/or light intensity used during the light-based 3D printing process.[25,31] These highly favorable properties of PGSA coupled with its compatibility with the DLP-based 3D printing system make this biomaterial a candidate worth exploring to fabricate a complex muscle–tendon scaffold with zonal stiffness regions mimicking those of native muscle–tendon tissue.

The aim of this study is to develop a physiologically relevant *in vitro* MTJ model that replicates the morphological and mechanical complexity of the native muscle–tendon unit. The cellular response of C2C12 muscle cells and NIH/3T3 fibroblasts on 3D-printed PGSA scaffolds with a microarchitecture that reflects physiological conditions and varying degrees of mechanical heterogeneity *in vitro* were thoroughly evaluated. First, morphological characterization of the native muscle–

tendon tissue with imaging-based techniques (*e.g.*, SEM and TEM imaging) was performed and the local mechanical properties of native muscle–tendon tissue were measured with nanoindentation. These data were then used to fabricate a physiologically informed muscle–tendon scaffold design with tissue-derived microstructure and material properties. In addition, Young's modulus values obtained from native muscle, MTJ, and tendon were entered into a previously described machine learning model[35] to optimize printing parameters to fabricate a PGSA muscle–tendon scaffold with mechanical properties that accurately reflect those of native muscle, MTJ, and tendon. PGSA scaffolds with microarchitecture and mechanical properties mimicking those of native muscle–tendon tissue were successfully fabricated, and key outcomes such as the expression of MTJ-related genes were evaluated in relation to PGSA-based constructs with differing stiffness conditions. We hypothesized that 3D-printed, physiology-informed PGSA-based scaffolds possessing zonal stiffness regions similar to those present in native muscle–tendon tissue would provide structural and biophysical cues that can facilitate the formation of a stable muscle–tendon junction and the expression of MTJ-related markers. Overall, this work presents a novel approach for the utilization of DLP-based 3D printing for engineering the muscle–tendon unit *in vitro*.

2. Materials and methods

2.1. Materials

Acryloyl chloride, diphenyl(2,4,6-trimethylbenzoyl)phosphine oxide (TPO), triethylamine (TEA), anhydrous dichloromethane (DCM), tetrahydrofuran (THF), and tartrazine were purchased from MilliporeSigma (St Louis, MO). Glycerol, ethyl acetate, and sebacic acid were purchased from Fisher Scientific (Waltham, MA). Dulbecco's modified Eagle's medium (DMEM), Normocin™, fetal bovine serum (FBS), and penicillin/streptomycin (P/S) were purchased from Thermo Fisher Scientific (Waltham, MA).

2.2. PGS synthesis

The poly(glycerol sebacate) (PGS) synthesis protocol followed a previously established protocol.[31] Glycerol and sebacic acid were mixed at a 1 : 1 equimolar ratio under an argon atmosphere at 140 °C for 1 h in a round bottom flask. Afterwards, the temperature was reduced to 120 °C, and the pressure was reduced to 35 Pa to allow for the polycondensation reaction to be carried out. The polycondensation reaction was carried out for the next 15 h at 120 °C and 35 Pa.

2.3. PGS acrylation

The acrylation of PGS followed a previously established protocol.[31] Briefly, 300 ml of DCM was added to 30 g of PGS to dissolve it at room temperature under argon gas and constant stirring. Once 30 g of PGS is completely dissolved in the DCM solvent, 30 mg of DMAP was added to the flask and the temp-

erature was reduced to 0 °C over 10 min by immersing the round bottom flask containing PGS and DCM in an ice bath. Once the temperature was reduced and maintained at 0 °C, 7 ml of TEA was added in a dropwise manner into the reaction flask. This was then followed by a dropwise addition of 3.3 ml of acryloyl chloride for acrylation. The acrylation reaction was allowed to continue for the next 24 h under room temperature and argon gas in the dark. After that, DCM was removed from the solution by rotary evaporation at 40 °C under ultimate vacuum. 200 ml of excess ethyl acetate was then added to the solution to precipitate TEA out. The PGSA solution was then filtered and subjected to rotary evaporation at 45 °C and 5 Pa to evaporate excess ethyl acetate. Once that was finished, PGSA was stored at −20 °C in the dark until use. The PGSA prepolymer solution that was used in this study was synthesized from the same batch and from the same flask as the PGSA prepolymer used in the previously published literature with 57% degree of acrylation.[31,35] The synthesized PGSA prepolymer had a weight average molecular weight (M_w) of 2686 (±1.523%) and number average molecular weight (M_n) of 922.4 (±7.688%), as determined by gel permeation chromatography (GPC) using tetrahydrofuran (THF) as solvent, and a polydispersity index (PDI) of 2.9.

2.4. Photopolymerizable printing solution preparation

PGSA was thawed on a heating block at 37.5 °C. The photopolymerizable PGSA-based printing solution was prepared by mixing 96% (w/v%) PGSA prepolymer solution with 0.01% (w/v%) tartrazine (photoinhibitor) and 4% (w/v%) TPO (photoinitiator) under vortex prior to 3D printing.

2.5. DLP-based 3D printing

The DLP-based 3D printing system consisted of a 385 nm light source, a digital micromirror device (DMD) chip, a series of projection optics for patterned light guidance, a prepolymer resin reservoir loaded onto a static stage, a motion-controlled probe with a methacrylated coverslip that continuously moves up in the *z*-direction, and a computer system synchronized to the hardware for controlling the digital pattern, printing speed, light intensity, and exposure time used for 3D printing (Fig. 1). The digital patterns for 3D-printed scaffolds were designed in Fusion360 (San Francisco, CA) and output as .STL files, which were then sliced into 2D digital masks using an in-house-developed MATLAB (Mathworks, Natick, MA) script.

To 3D-print a scaffold, first, the 385 nm light from the light source is projected onto the DMD chip. The DMD chip, which is synchronized to the computer system, consists of 4 million micromirrors that flip on and off to generate patterned light corresponding to the digital patterns that are sequentially uploaded through the in-house-developed 3D printing software. The patterned light that reflects off the DMD chip is then guided through a series of projection lenses into a polydimethylsiloxane (PDMS)-coated prepolymer reservoir containing the PGSA prepolymer. The motion-controlled probe moves up in the *z*-direction for 200 μm, then moves down 100 μm, to allow for the first 100 μm thick PGSA base construct to be
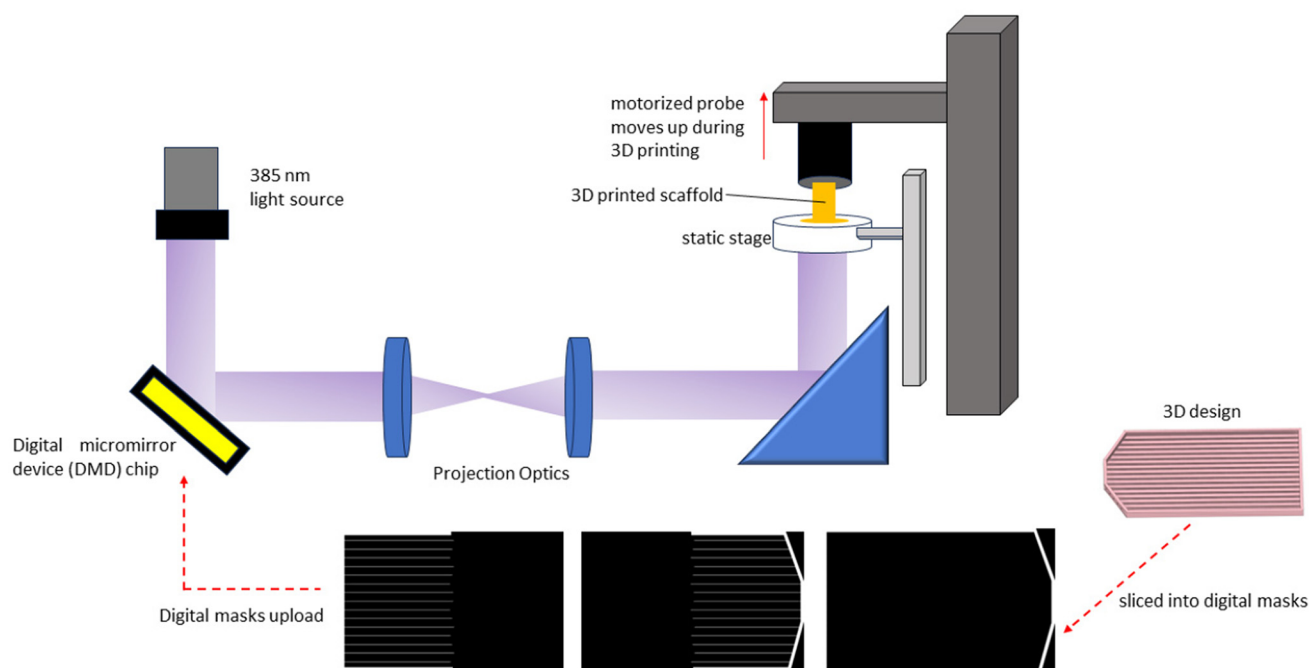
Fig. 1 Schematic of the DLP-based 3D printing system. Digital masks were sequentially uploaded to the synchronized, computerized 3D printing system. The DMD chip then adjusted their micromirror orientation according to the digital pattern uploaded into the synchronized 3D printing system. The 385 nm light projected from the light source was reflected off the DMD chip as patterned light and was projected through a series of projection lens to ultimately reach the focal plane within the static stage that contained the prepolymer reservoir. PGSA prepolymer was then photo-crosslinked into a 3D-printed structure as the motorized probe moved up in a layer-by-layer fashion during the printing process.

photopolymerized at the focal plane in a layer-by-layer fashion. Once the PGSA base layer is 3D printed, the probe containing the 3D-printed first layer is then moved up again by 100 μm to allow for a second layer to be printed at the focal plane, generating 100 μm thick microchannel walls on top of the first layer of the scaffold. Lastly, the probe is moved up again by 100 μm to allow for a third layer meant to serve as the 100 μm thick outer walls to be printed at the focal plane.

Once the 3D printing process was complete, the PGSA scaffolds were rinsed in isopropyl alcohol (IPA) to remove unreacted monomer, then DI water to dilute the IPA, and ultimately samples were placed in phosphate-buffered saline (PBS).

2.6. Rat tissue isolation

MTJs from the Achilles tendon were harvested from 6-month-old Lewis rats immediately postmortem. The MTJ was visually identified and was transected with 1 mm of muscle proximal and 1 mm of tendon distal to the site. The tissue containing muscle, myotendinous junction, and tendon was excised as a 3 mm × 3 mm × 1 mm rectangle using scissors. MTJs were immediately stored in PBS and kept at 4 °C prior to mechanical testing.

2.7. Nanoindentation of native rat muscle, myotendinous junction, tendon, and 3D-printed scaffolds

All animal procedures were approved by the University of California San Diego Institutional Animal Care and Use Office.

The native rat tissues (3 mm × 3 mm × 1 mm) and PGSA rectangular specimens (3 mm × 3 mm × 1 mm) were tested using a Piuma nanoindenter (Optics11, Amsterdam, The Netherlands) to measure the Young's modulus of the isolated muscle, myotendinous junction, and tendon. The tissue samples were mounted at the bottom of a Petri dish using super glue and submerged in PBS at room temperature. A nanoindenter spherical probe with a cantilever stiffness of $k = 4.14$ N m^{-1} and a tip radius of 3 μm was used. For each tissue sample, nanoindentation was carried out in a 5 × 5 matrix (25 indentations) and the average was calculated for each tissue sample (muscle, myotendinous junction, and tendon). Nanoindentation data were analyzed based on the Hertz contact model[36] under the assumption that the Poisson's ratio was 0.5.[37,38] For the rat muscle tissue, $n = 9$ muscle samples were tested. For the rat myotendinous junction, $n = 6$ samples were tested. For the rat tendon tissue, $n = 7$ samples were tested. For the PGSA specimens, $n = 6$ samples were tested.

2.8. Utilization of machine learning tool to generate printing parameter combinations

Once the Young's moduli of native tissue samples such as muscle, MTJ, and tendon were obtained, a previously described neural network (NN) model[35] was used to inform printing parameters that would generate PGSA scaffolds with user-defined stiffness values that correspond to native tissue stiffness. Previously, we mechanically tested the stiffness of

PGSA scaffolds printed with various printing parameter combinations and trained an NN model with these data.[35] The developed NN model was demonstrated to be able to accurately predict scaffold stiffness within the reasonable printing parameter range. In addition, the model was also able to suggest a combination of parameters that could reach desired target stiffness range from 58 kPa to nearly 1.2 MPa. The developed model was verified by 3D printing with suggested NN-generated parameters for stiffness values that were previously unseen from the training data. The R^2 between the target stiffness and measured stiffness values was 0.95. Since the same biomaterial platform and printing technique were used in this study, the fully trained NN model from our previous study[35] could be directly applied to fabricate PGSA-based scaffolds with mechanical properties matching those of native tissue by generating the corresponding set of printing parameters.

2.9. Cell culture and seeding

C2C12 cells (ATCC, Manassas, VA) and NIH/3T3 cells (ATCC, Manassas, VA) were expanded in growth media containing high-glucose DMEM, 10% FBS, 1% P/S, and 0.2% Normocin™. C2C12 cells and NIH/3T3 cells used in this study were at passage 6. Before seeding the cells onto the PGSA scaffolds, the 3D-printed PGSA scaffolds were primed overnight in high-glucose DMEM at 37 °C in an incubator. A 1 mm thick PDMS slab was placed in the middle of the PGSA scaffolds to prevent the cell droplets from overflowing from one side to the other.

C2C12 cells were seeded as a 10 μl droplet on one end of each PGSA scaffold while NIH/3T3 cells were seeded as a 10 μl droplet on the other end of each PGSA scaffold. The total seeding density for each cell type was 5000 cells per scaffold. Then, the PGSA scaffolds seeded with cells were incubated at 37 °C for 2 h. After 2 h, the cells were checked under the microscope to ensure that the cells were able to attach to the PGSA scaffolds. Then, 500 μl of complete growth medium (high-glucose DMEM, 10% FBS, 1% P/S, 0.2% Normocin™) was added into each well. After 24 h, the PDMS slab was removed from the middle of each scaffold. The cells were maintained in complete growth media for 1 and 7 days for cell viability testing. The cells were maintained in complete growth media for 14 days for RT-qPCR gene expression analysis. The cells were maintained in complete growth media for 14 days for immunostaining.

2.10. Cell viability testing

C2C12 cells and NIH/3T3 cells were seeded onto the 3D-printed PGSA slabs the stiffness of which corresponds to native muscle, MTJ, and tendon stiffness values. At days 1 and 7, the cell-seeded scaffolds were rinsed with PBS and stained with calcein AM (Biotium, Fremont, CA) and ethidium homodimer-1 (Biotium, Fremont, CA) according to the manufacturer's protocol. The seeded PGSA scaffolds were imaged using a Leica widefield fluorescence microscope (Leica DMI-6000, Wetzler, Germany), and the viability of the cells was analyzed using ImageJ software.

2.11. Immunofluorescence staining of cell markers

At each timepoint, the scaffolds were rinsed three times in PBS. Then, the scaffolds were fixed in 4% paraformaldehyde (PFA) solution for 30 min at room temperature on a shaker. Once the scaffolds were fixed with 4% PFA, the scaffolds were rinsed again three times in PBS. After PBS rinsing, the scaffolds were blocked and permeabilized in a block/perm solution consisting of 5% (w/v) bovine serum albumin (BSA) (GeminiBio, West Sacramento, CA) and 0.2% (w/v) Triton X-100 (MilliporeSigma, St Louis, MO) in PBS on a shaker for 1 h. After 1 h, the scaffolds were incubated with rabbit monoclonal anti-integrin beta 1 antibody (1 : 200, ab179471, Abcam) diluted in 5% BSA solution or rabbit polyclonal anti-collagen I antibody (1 : 200, ab21286, Abcam) diluted in 5% BSA solution overnight at 4 °C. Once incubated overnight at 4 °C, the scaffolds were rinsed three times in PBS and incubated with CF-555 goat anti-rabbit secondary antibody (1 : 200, Biotium) for 1 h on a shaker. After that, the scaffolds were rinsed again three times in PBS on a shaker. After that, the scaffolds were stained with CF-647 conjugated phalloidin (1 : 200, Biotium) for 1 h followed by three PBS washes. All samples were immediately imaged with a Leica SP8 confocal microscope after staining.

2.12. RNA isolation and reverse transcription-polymerase chain reaction (RT-qPCR)

Cell-seeded co-culture PGSA scaffolds were washed in PBS and then incubated with TrypLE (Thermo Fisher Scientific) for 5 min. Once done, the cells were diluted with DMEM, centrifuged, and resuspended in 2% FBS. The cells were then filtered through a 40 μm cell strainer and transferred to FACS tubes. After FAC sorting, mCherry-C2C12 cells and NIH/3T3 cells were sorted into separate 15 ml conicals. The mCherry-C2C12 cells and NIH/3T3 cells sorted by FACS were then centrifuged and resuspended in 300 μl of TRIzol reagent (Life Technologies).

To make sure that enough RNA was collected from the PGSA scaffolds, 144 samples were combined and extracted together for each condition per replicate. Three replicates were collected per condition (n = 3). The total RNA was extracted using a Direct-zol RNA MicroPrep Kit (R2060, Zymo Research). The RNA concentration of each sample was verified using a Tecan plate reader. The extracted RNA samples were immediately stored at −80 °C until use.

For cDNA synthesis, the extracted RNA samples were converted to cDNA using the ProtoScript® First Strand cDNA Synthesis Kit (E6300, New England Biolabs Inc.) and QuantStudio™ 3 Real-Time PCR system. NCBI primer-BLAST was used to design the primers, which were subsequently purchased from Integrated DNA Technologies. RT-qPCR was performed using the Luna® Universal qPCR Master Mix (M3003, New England Biolabs Inc.) and QuantStudio™ 3 Real-Time PCR system. Gene expression of each specific gene was determined by normalizing the threshold cycle (C_t) values against those of the housekeeping gene, which was glyceraldehyde 3-phosphate dehydrogenase (GAPDH) in this case. Primer information can be found in ESI Table 1.†

2.13. Statistics

The results are presented as mean ± standard deviation (SD). All statistical analyses were performed using GraphPad Prism 9 (La Jolla, CA). One-way analysis of variance (ANOVA) with Sidak *post hoc* tests was used to determine differences between experimental groups. Data are reported as mean ± standard deviation and are considered statistically significant when $p < 0.05$. An Inter-rater Correlation Coefficient (ICC; 2,1) was run to investigate the agreement between target and measured stiffness. The ICC was calculated using SPSS Version 20.0 (IBM Corporation, Armonk, NY).

3. Results and discussion

3.1. Investigation of the native muscle–muscle tendon microarchitecture

To fabricate a physiologically relevant muscle–tendon scaffold *via* DLP-based 3D printing, the morphology of the native muscle–tendon microarchitecture must first be investigated.

Native muscle–tendon tissue was freshly isolated and dissected from a recently sacrificed rat's Achilles tendon. The freshly isolated rat muscle–tendon tissue was then subjected to SEM and TEM imaging processes to generate high resolution images of the rat's native muscle–tendon microarchitecture (Fig. 2).

The MTJ is the junction that serves as the interface between the muscle and tendon tissues.[4] Force is transmitted from the muscle to the tendon through the MTJ, whose main function is to help minimize focal stress by increasing the interfacial surface area between muscle and tendon.[3,4] The mechanical properties of MTJ are between those of muscle and tendon, and serve to promote the gradual stiffness transition between the softer muscle region and stiffer tendon region. The tendon region is primarily composed of ECM and bundles of collagen fibers. The muscle region is primarily cell-based and is composed of bundles of myofibers. SEM of the MTJ demonstrates finger-like interdigitations with a great surface area (Fig. 2A). TEM of the MTJ demonstrates higher resolution morphology of the MTJ with finger-like projections connecting the tendon ECM to the muscle (Fig. 2D). The finger-like projections of the
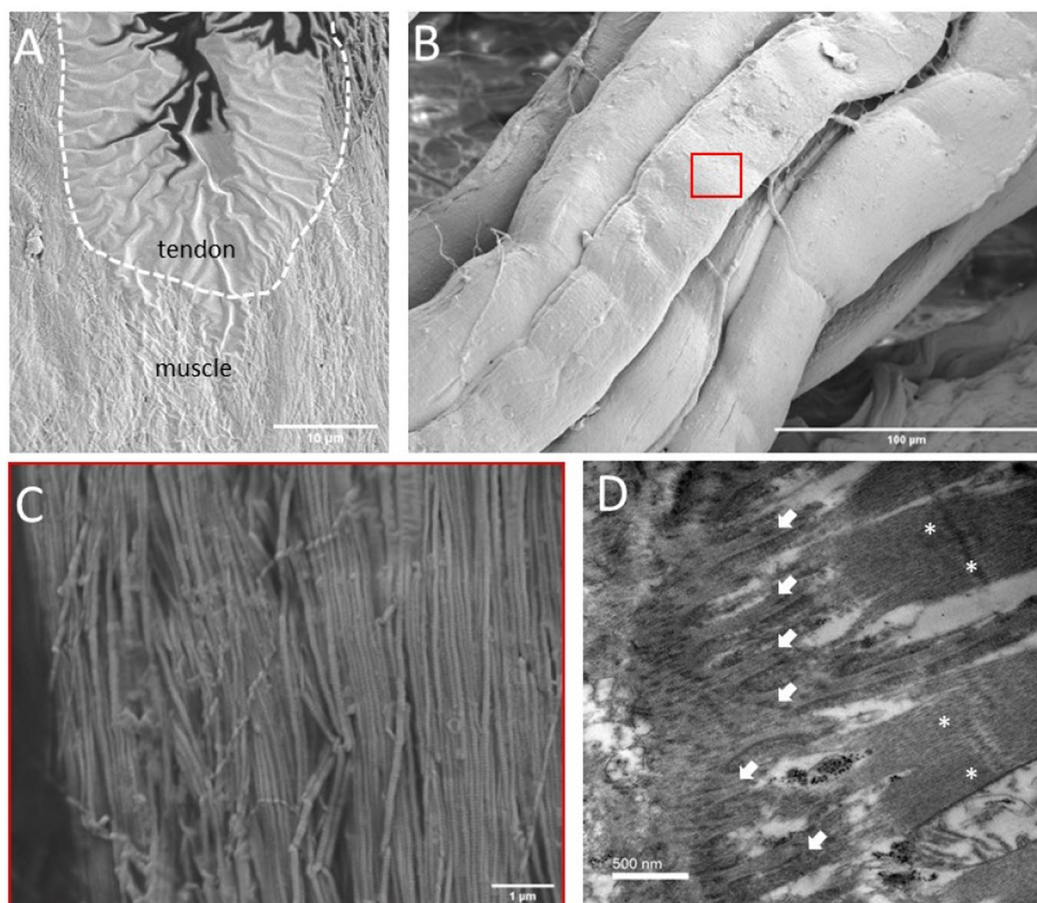
Fig. 2 Structure of the muscle–tendon tissue. (A) Scanning electron microscopy (SEM) image of native muscle–tendon tissue. Dashed lines indicate the myotendinous junction that separates the muscle from the tendon (scale bar = 10 μm). (B) SEM image of native muscle bundle isolated from a rat's Achilles tendon (scale bar = 100 μm). (C) SEM image of myofibrils, which is the zoomed-in image of the indicated area from (B) (scale bar = 1 μm). (D) Transmission electron microscopy (TEM) image of the native muscle–tendon tissue (scale bar = 500 nm). Note the region of the MTJ (arrows) and the bundles of myofibrils (*).

MTJ are crucial to the stability of the muscle–tendon structure and force transmission ability, as the large surface area of the interdigitations allows for the reduction of stress concentrations and smooth transition of the tissue stiffness zones.

3.2. Mechanical properties of native muscle–tendon tissue

Due to the small interfacial areas of the MTJs, it is extremely challenging to measure their mechanical properties using conventional mechanical testing methods without the influence of the nearby adjacent tissues.[19,39–42] To circumvent the challenges associated with using conventional methods to test the stiffness of the MTJ, nanoindentation was chosen to test the native MTJs. Nanoindentation is an emerging mechanical testing technology that allows for the mechanical characterization of biological tissues by making small-scale indentations into the sample to measure the Young's modulus of a user-defined local area of the tissue of interest.[43–47] This enables the investigation into the hyperlocal mechanical properties of tissue samples that possess hierarchical multi-scale organization such as the MTJ.[44]
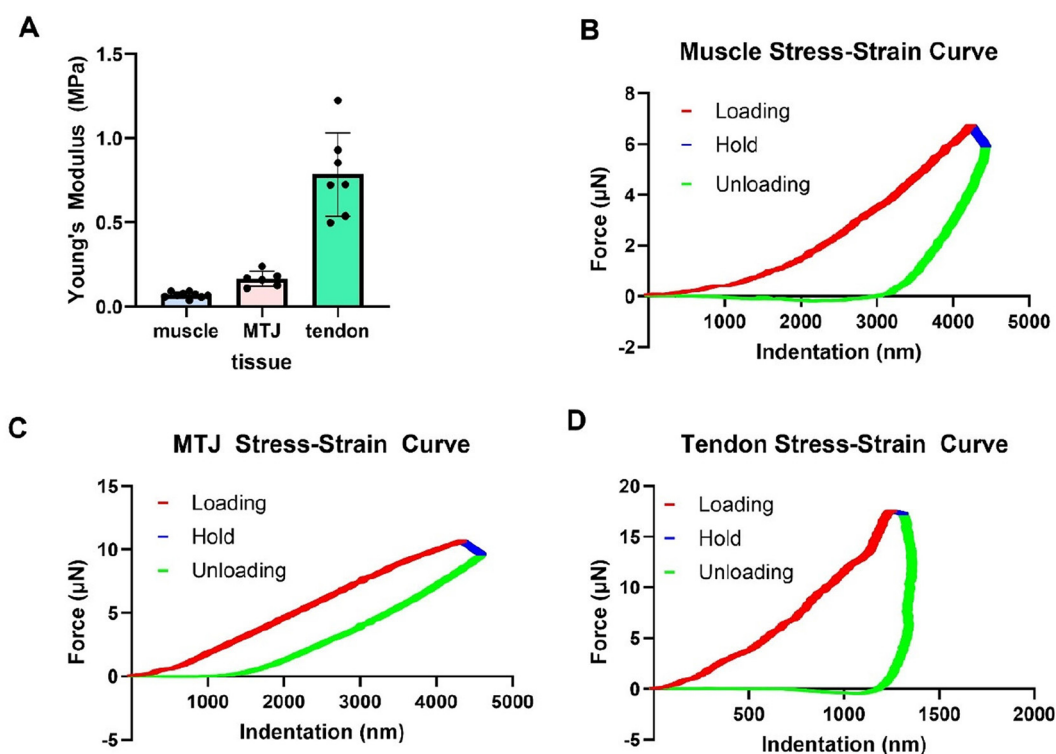
The native muscle, MTJ, and tendon tissues isolated from a rat's Achilles tendon were glued into a Petri dish, immersed in PBS, and subjected to nanoindentation mechanical testing. The Young's moduli of native rat muscle, MTJ, and tendon were found to be 68.82 ± 16.66 kPa (Fig. 3A and B), 163.4 ± 45.52 kPa (Fig. 3A and C), and 785.0 ± 248.2 kPa (Fig. 3A and

D), respectively. These results confirm that the native muscle–tendon tissue possesses heterogeneous mechanical properties consisting of zonal stiffness regions whose stiffness increases in the order of muscle, MTJ, and tendon.

3.3. Engineering design of a physiologically informed muscle–tendon scaffold

After the morphology of native rat muscle–tendon tissue was investigated *via* SEM and TEM, the native tissue microstructures were used to inform an engineered scaffold design consisting of simplified geometries to have controllable, repeatable microstructures capable of packing C2C12 cells and NIH/3T3 cells *in vitro* into a highly organized structure with anisotropic alignment that mimics that of native muscle–tendon tissue (Fig. 4A and B).

The collagen fibers in the tendon ECM and the muscle fibers were simplified to 300 µm microchannels to allow for the packing and alignment of tenocytes/fibroblasts and muscle cells. The finger-like invaginations as seen in native MTJ (Fig. 2D) were transformed into zigzag patterns in the middle of the scaffold to help increase the surface area for muscle–tendon cell interactions. In addition, the outer walls with a width of 125 µm and a height of 300 µm surrounding the scaffold perimeter were added into the scaffold design to contain the seeded cell droplets within the muscle and tendon

Fig. 3 Nanoindentation testing results of native muscle–tendon tissue. (A) Young's modulus measurements of native rat's muscle, MTJ, and tendon through the nanoindentation technique. (B) An example stress–strain curve of native rat muscle tissue that underwent nanoindentation testing. (C) An example stress–strain curve of native rat MTJ that underwent nanoindentation testing. (D) An example stress–strain curve of native rat tendon tissue that underwent nanoindentation testing.
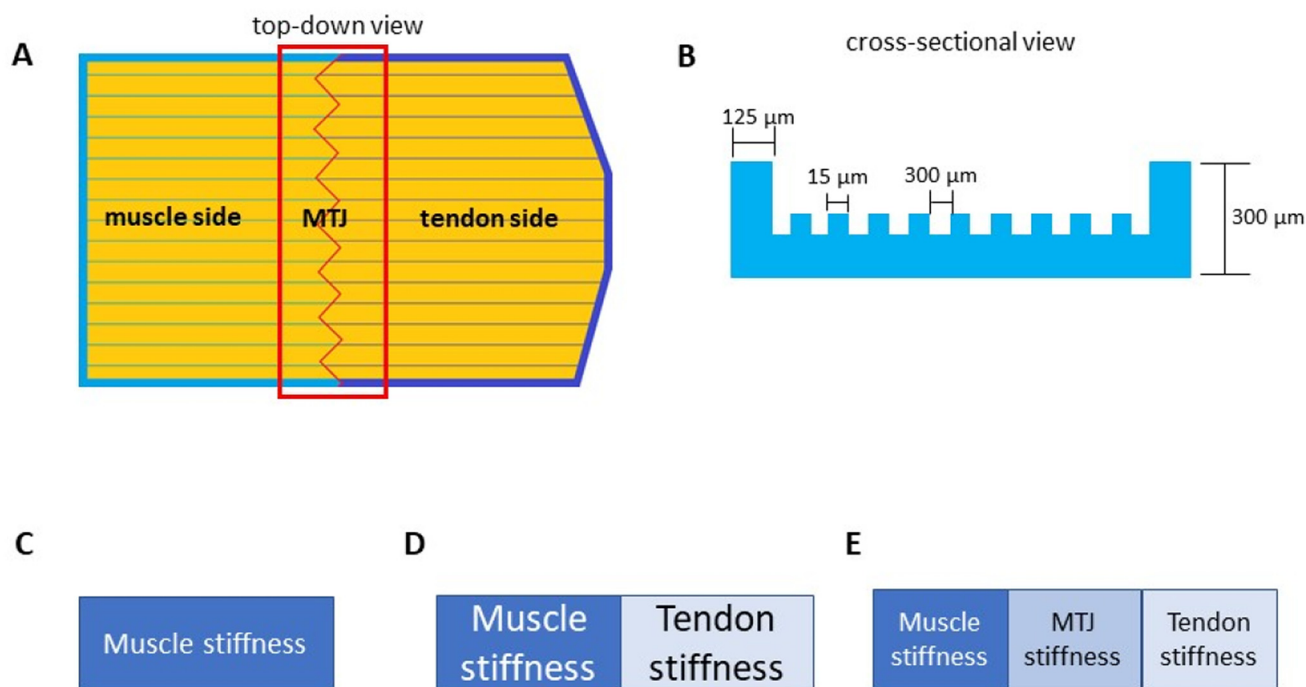
Fig. 4 Engineered design of muscle–tendon scaffold. (A) Top–down view of the PGSA muscle–tendon scaffold used in this study. (B) Cross-sectional view of the PGSA muscle–tendon scaffold used in this study and its dimensions. (C) PGSA muscle–tendon scaffold designed to possess one stiffness region mimicking that of native rat muscle in its entirety. (D) PGSA muscle–tendon scaffold designed to possess two stiffness regions mimicking those of native rat muscle and tendon. (E) PGSA muscle–tendon scaffold designed to possess three stiffness regions mimicking those of native rat muscle, MTJ, and tendon.

regions without leaking out from the scaffolds during the cell-seeding and cell-culturing process.

To design a tissue-engineered scaffold for musculoskeletal tissue engineering applications, it is of crucial importance to fabricate scaffolds whose stiffness matches that of the native tissue of interest, since microscale biophysical and topographical cues play a significant role in the migration, alignment, proliferation, and differentiation of cells through stiffness-mediated cellular responses.[48–51] To investigate how PGSA scaffolds with varying mechanical properties influence cellular responses, the PGSA muscle–tendon scaffolds were fabricated under three distinct conditions.

3.3.1. Uniform stiffness scaffold (PGSA-1STN). This scaffold possesses a Young's modulus designed to mimic that of native rat muscle tissue throughout the entire area (Fig. 4C).

3.3.2. Bimodal stiffness scaffold (PGSA-2STN). This scaffold features two discrete stiffness regions. The first half mimics the Young's modulus of the native rat muscle tissue, while the second half is designed to replicate the Young's modulus of the native rat tendon tissue (Fig. 4D).

3.3.3. Transitional stiffness scaffold (PGSA-3STN). This scaffold includes transitional stiffness zones with three distinct regions. The first region mimics the Young's modulus of the native rat muscle tissue, the middle region simulates the Young's modulus of the native rat MTJ tissue, and the third region replicates the Young's modulus of the native rat tendon tissue (Fig. 4E).

3.4. Determination of DLP-based 3D printing parameters for native tissue stiffness mimicry

Previous studies have shown that the Young's modulus of DLP-based 3D-printed scaffolds can be modulated by the adjustment of various 3D printing parameters such as exposure time and light intensity.[25,31,52] Using a light-based DLP 3D printing platform, both the light intensity and the exposure time are the two important printing parameters that can be adjusted to fabricate 3D-printed scaffolds with a user-defined range of mechanical properties from the same starting prepolymer resin. The rate of photopolymerization in light-based 3D printing has been shown to follow a direct power law relationship with light intensity.[30,53–56] Increased light intensity exposes the photopolymerizable prepolymer resin to more photons per exposure duration, allowing for the generation of more free radicals and acceleration of the photopolymerization rate. This leads to a higher crosslinking density that restricts the polymer chain movement and increases the stiffness. Additionally, the exposure time has been shown to directly influence the crosslinking density, with longer exposure times resulting in more complete crosslinks and a higher stiffness.[30,55,56] Previously, an extensive range of DLP-based printing parameters and their corresponding stiffness values from 3D-printed PGSA scaffolds were investigated,[35] and the generated data were used to develop a neural network model that allows for precise stiffness control of 3D-printed PGSA-

based scaffolds. Based on these results,[35] the neural network (NN) model was able to generate DLP-based 3D printing parameters for 3D printing PGSA-based scaffolds with user-defined stiffness values with great accuracy (R^2 = 0.95).

Using this NN model, user-defined Young's moduli based on nanoindentation testing of native rat muscle, MTJ, and tendon tissues were input into the NN model to generate predicted 3D printing parameters that would yield stiffness values matching those of native tissues. Once the PGSA scaffolds were printed according to the artificial intelligence (AI)-generated parameters, their stiffness values were verified by nanoindentation testing and compared to the user-defined stiffness input to ensure that the stiffness of the printed scaffolds matches that of the native tissue. The resulting AI-generated parameters as well as the measured stiffness of the 3D-printed PGSA-based scaffolds are listed on Table 1 and compared in Fig. 5.

The ICC analysis between the target stiffness and actual measured stiffness in 3D-printed scaffolds yielded ICC = 0.997. This indicates the AI model was able to generate DLP-based 3D printing parameters for PGSA scaffolds to yield PGSA scaffolds with intended stiffness values matching those of native-muscle tendon tissue with a high degree of accuracy. This allows us to precisely fabricate PGSA muscle–tendon scaffolds possessing heterogeneous mechanical properties matching those of native muscle–tendon tissue through a layer-by-layer 3D printing process with user-defined printing parameters instead of having to perform a more complex scaffold fabrication approach such as creating a composite material scaffold or modifying different regions with biomaterials possessing different acrylation ratios.[13,17,18]

### 3.5. 3D printing of PGSA-based muscle–tendon scaffolds

Muscle–tendon scaffolds were 3D printed under the three muscle–tendon PGSA scaffold conditions using an in-house-developed DLP-based 3D printer in a layer-by-layer fashion, following the process outlined in the Materials and methods section. No artificial structural interfaces were observed between the different zones after printing (Fig. 6). The order of the masks applied for each simulated MTJ condition is depicted in ESI Fig. S1–S3.†

### 3.6. Cell viability on 3D-printed PGSA scaffolds with differing stiffness values

Although PGSA has been previously demonstrated to be biocompatible with muscle progenitor cells and fibroblasts,[31,33] it is crucial to investigate the biocompatibility of PGSA scaffolds printed at varying stiffness values to ensure that PGSA-1STN, PGSA-2STN, and PGSA-3STN scaffolds support the viability of

Table 1 The AI-generated printing parameters, corresponding target stiffness, and measured stiffness values

3D printing system	AI-generated parameters	Target stiffness (kPa)	Measured stiffness (kPa)
DLP-based	Light intensity: 12.40 mW cm^{-2} Exposure time: 47 s	68.62 (mean of measured native muscle stiffness)	68.39 ± 4.129
	Light intensity: 13.70 mW cm^{-2} Exposure time: 49 s	163.4 (mean of measured native MTJ stiffness)	157.9 ± 12.67
	Light intensity: 15.17 mW cm^{-2} Exposure time: 59 s	785.0 (mean of measured native tendon stiffness)	802.7 ± 39.64
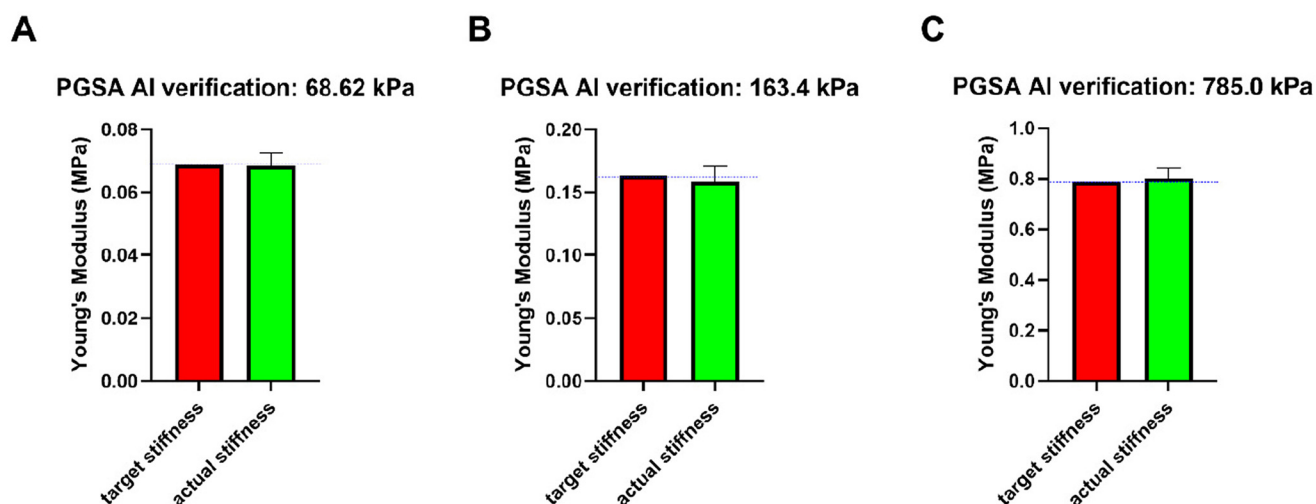
Fig. 5 Machine learning results and verification. Comparisons between the user-defined stiffness values based on (A) the mean of measured native rat muscle Young's modulus, (B) the mean of measured native rat MTJ Young's modulus, and (C) the mean of measured native rat tendon Young's modulus *versus* the DLP-based 3D-printed sample stiffness using the printing parameters generated by the AI model for 68.62 kPa, 163.4 kPa, and 785.0 kPa, respectively. The ICC analysis between the target stiffness and actual measured stiffness in 3D-printed scaffolds yielded ICC = 0.997.
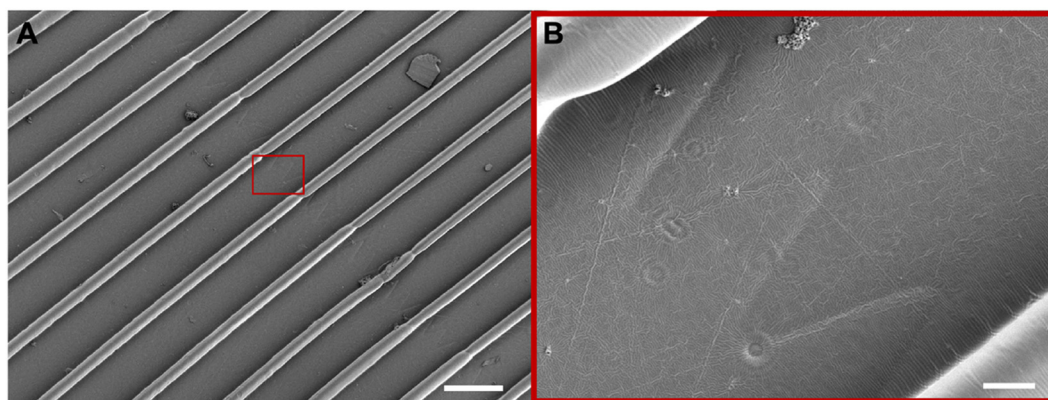
Fig. 6 SEM images of the zonal scaffold. (A) 60× SEM image of the muscle–tendon PGSA scaffold. Scale bar = 200 μm. (B) 550× SEM image of the muscle–tendon PGSA scaffold. Scale bar = 200 μm. From SEM it is evident that the surface is continuous and there are no artificial structural interfaces between zones.
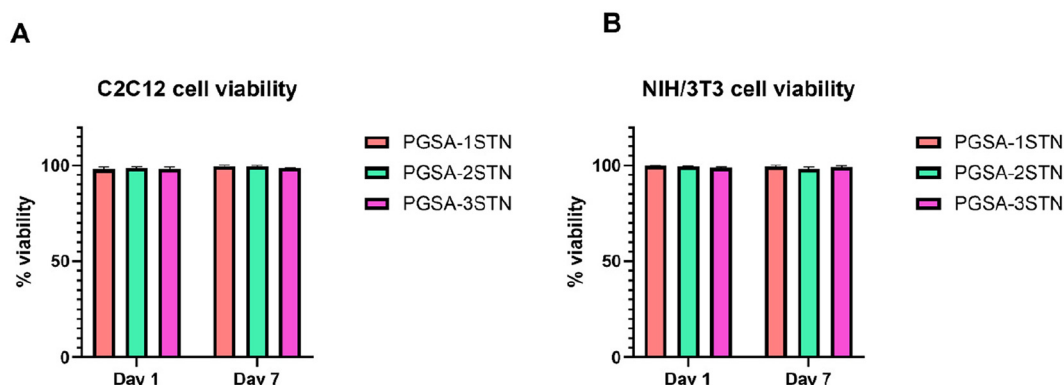
Fig. 7 Cell viability of C2C12 and NIH/3T3 cells seeded on PGSA printed at different stiffness values. Cell viability of (A) C2C12 and (B) NIH/3T3 cells seeded on PGSA-1STN, PGSA-2STN, and PGSA-3STN on day 1 and day 7 timepoints.

both C2C12 muscle cells and NIH/3T3 fibroblast cells in long-term culture. The cell viability testing of C2C12 cells and NIH/3T3 cells seeded onto 3D-printed PGSA scaffolds with stiffness values corresponding to 68.39 ± 4.129 kPa (native rat muscle stiffness), 157.9 ± 12.67 kPa (native rat MTJ stiffness), and 802.7 ± 39.64 kPa (native rat tendon stiffness) showed high cell viability (>95%) for all stiffness conditions at day 1 and day 7 after cell seeding (Fig. 7; ESI Fig. S4†).

3.7. Expression of MTJ-related markers on seeded PGSA scaffolds

After 14 days in culture, the PGSA constructs were immunostained against MTJ-related markers such as Itgb1 and collagen I to investigate the development of the tissue at the C2C12–NIH/3T3 interface (Fig. 8) across PGSA constructs with various stiffness conditions. Itgb1 is a junction protein that is highly expressed and concentrated at the MTJ and is an important MTJ component involved in the transmission of forces across the junction, as it links the actin cytoskeleton with tendon ECM.[57–59] Most of the tendon ECM is composed of hierarchical organizations of collagen fibers aligned in the same direc-

tion to aid in force transmission and loading and maintaining the structural integrity of the MTJ.[11,14] Collagen I is a principal ECM protein that is highly expressed at the MTJ and is continuous across the MTJ to help transmit forces that are generated from skeletal muscle across the tendon through the MTJ and to the bone.[11,14,60] Confocal images (Fig. 8) were taken at the engineered invaginations presented in the middle of the PGSA scaffold where C2C12 cells from one end of the scaffold interacted with NIH/3T3 fibroblasts from the other end of the scaffold.

For PGSA-1STN scaffolds, both MTJ-related markers Itgb1 and collagen I were present at the scaffold junction (Fig. 8A and B). The same observations are also made for PGSA-2STN (Fig. 8C and D) and PGSA-3STN (Fig. 8E and F) scaffolds. Under all scaffold conditions, extensive expression of Itgb1, which is a junction protein linking F-actin to ECM, can be observed qualitatively at the junction of all scaffold types (Fig. 8A, C and E). Collagen I, a principal ECM protein across the MTJ junction, was observed to be expressed and present across the length of the junction in all PGSA muscle–tendon scaffold types (Fig. 8B, D and F). In addition, a high degree of
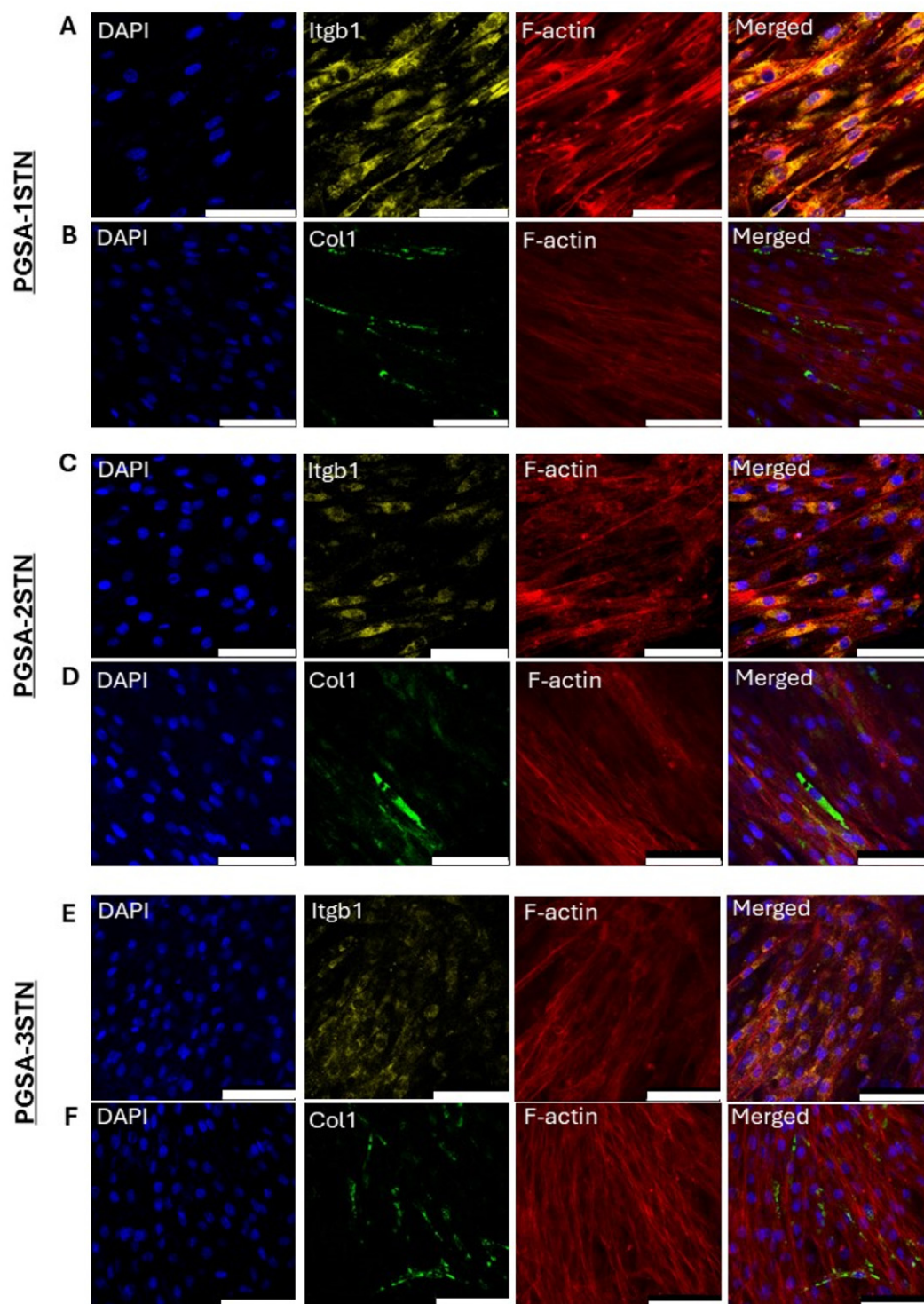
Fig. 8 Day 14 immunostaining of MTJ-related markers within PGSA-1STN, PGSA-2STN, and PGSA-3STN scaffolds. (A and B) Confocal images taken at the finger-like junction of the PGSA-1STN scaffold where C2C12 cells and NIH/3T3 cells interacted with each other on day 14. (A) Cells at the junction were stained for Itgb1, which was an MTJ-related marker. (B) Cells at the junction were stained for Col1, which was another MTJ-related marker. (C and D) Confocal images taken at the finger-like junction of the PGSA-2STN scaffold where C2C12 cells and NIH/3T3 cells interacted with each other on day 14. (C) Cells at the junction were stained for Itgb1, which was an MTJ-related marker. (D) Cells at the junction were stained for Col1, which was another MTJ-related marker. (E and F) Confocal images taken at the finger-like junction of the PGSA-3STN scaffold where C2C12 cells and NIH/3T3 cells interacted with each other on day 14. (E) Cells at the junction were stained for Itgb1, which was an MTJ-related marker. (F) Cells at the junction were stained for Col1, which was another MTJ-related marker. Scale bar = 100 μm.

cellular alignment, as indicated by F-actin expression, can be observed under all scaffold conditions (Fig. 8). Furthermore, multinucleation indicative of skeletal muscle differentiation can be observed for cells grown under all PGSA construct conditions (Fig. 8). Interestingly, we may also speculate that the seeded NIH/3T3 fibroblasts have fused to the differentiated C2C12 muscle fibers, as it has been previously demonstrated that fibroblasts possess dual identity that allows them to express myogenic characteristics and fuse into muscle fibers along the MTJs.[9,61]

To identify and quantify the extent of MTJ-related gene expression to investigate the effect of how PGSA constructs with one stiffness zone, two stiffness zones, and three stiffness zones influence MTJ-related gene expression in C2C12 and NIH/3T3 cells, RT-qPCR gene expression analysis was performed to detect and quantify the expression of MTJ-related genes such as Itgb1, Tln1, and Col1a1 (Fig. 9) after 14 days of cell seeding. Since Tln1 is responsible for the maintenance of MTJs by connecting the actin cytoskeleton to integrins, Tln1 was chosen as the gene of interest.[62] To decouple the co-culture effect from the biophysical cues of zonal stiffness regions of 3D-printed PGSA scaffolds, mCherry-C2C12 and NIH/3T3 cells were sorted by FACS into separate conical tubes prior to RNA isolation and qPCR.

Among C2C12 cells, a significant increase in Itgb1 gene expression ($p < 0.01$) was observed for the cells seeded on
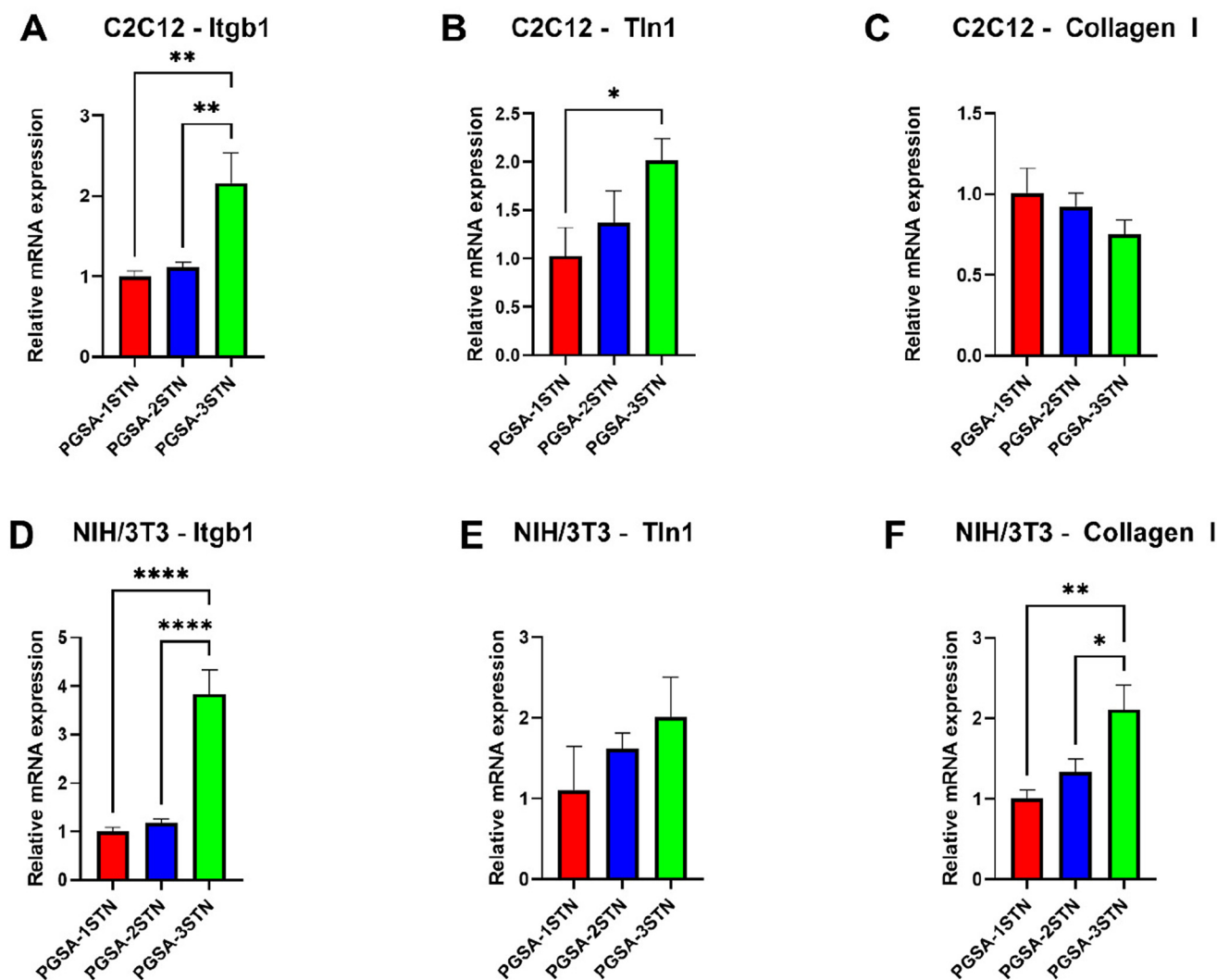
Fig. 9 mRNA expression of MTJ-related genes under various PGSA scaffold conditions. mRNA expressions of MTJ-related markers Itgb1, Tln1, and Col1a1 under (1) PGSA-1STN, (2) PGSA-2STN, and (3) PGSA-3STN conditions measured by real-time quantitative PCR (RT-qPCR). (A) Relative mRNA expression of Itgb1 expressed in C2C12 cells relative to PGSA-1STN control (muscle stiffness in its entirety; no zonal stiffness regions). (B) Relative mRNA expression of Tln1 expressed in C2C12 cells relative to PGSA-1STN control. (C) Relative mRNA expression of Col1a1 expressed in C2C12 cells relative to PGSA-1STN control. (D) Relative mRNA expression of Itgb1 expressed in NIH/3T3 cells relative to PGSA-1STN control. (E) Relative mRNA expression of Tln1 expressed in NIH/3T3 cells relative to PGSA-1STN control. (F) Relative mRNA expression of Col1a1 expressed in NIH/3T3 cells relative to PGSA-1STN control. $N = 3$ biological replicates and $n = 3$ technical replicates for each condition. P-Values were calculated using one-way ANOVA with Sidak *post hoc* test. *, $p < 0.05$; **, $p < 0.01$; ****, $p < 0.0001$.

PGSA-3STN scaffolds compared to those seeded on PGSA-1STN and PGSA-2STN (Fig. 9A). Among NIH/3T3 cells, the same trend in Itgb1 expression was also observed (Fig. 9D), whereby Itgb1 was significantly upregulated in PGSA-3STN compared to PGSA-1STN and PGSA-2STN ($p < 0.0001$). These results could suggest that the presence of MTJ-matching stiffness at the scaffold junction that served as the transitional stiffness region between the softer muscle side and stiffer tendon side of the scaffold may contribute to the upregulation of junction proteins such as Itgb1 as opposed to having a scaffold with just one stiffness value throughout or having a scaffold with two discrete stiffness regions (high stiffness region on one end and low stiffness region on the other end).

An increasing trend in the expression of Tln1, another MTJ-related protein, was also observed in C2C12 cells (Fig. 9B) and NIH/3T3 cells (Fig. 9E) cultured on PGSA-2STN and PGSA-3STN scaffolds, whereby the expression of Tln1 increased from PGSA-1STN to PGSA-2STN to PGSA-3STN, in an increasing order.

Among C2C12 cells, a reduction in the expression of collagen I was observed as the number of zonal stiffness regions possessing mechanical heterogeneity increases (Fig. 9C). Collagen I expression decreased from PGSA1-STN to PGSA-2STN to PGSA-3STN, in a decreasing order. The previous literature has shown that collagen type I mRNA expression decreases over the course of skeletal muscle differentiation.[10] These results could suggest that the presence of zonal stiffness regions in 3D-printed PGSA scaffolds may affect skeletal muscle differentiation.

Among NIH/3T3 cells, significant increase in collagen I expression was observed for NIH/3T3 fibroblasts seeded on PGSA-3STN scaffolds compared to that for those seeded on PGSA-2STN scaffolds ($p < 0.05$) and that for those seeded on PGSA-1STN ($p < 0.01$). These results suggest that the presence of transitional zonal stiffness regions present in PGSA scaffolds with stiffness regions matching those of native muscle, MTJ, and tendon could help stimulate an increase in the production of the MTJ-related ECM protein such as collagen I in fibroblasts.

4. Conclusion

In this study, the local mechanical properties of native rat muscle, MTJ, and tendon were investigated using nanoindentation, which allows one to precisely measure the local stiffness of biological tissue on a microscale. In addition, the morphology of native rat Achilles tendon with muscle proximal and tendon distal to the site was investigated using SEM and TEM imaging. By combining the mechanical data of native rat tissue with its morphological imaging data, we have developed a DLP-based 3D printing platform to model the muscle–tendon unit *in vitro* by fabricating a controllable, repeatable tissue-engineered PGSA-based elastomeric muscle–tendon scaffold with geometries and heterogeneous mechanical properties matching that of native muscle–tendon tissue with the

help of machine learning tools to accurately predict the printing parameters needed to generate scaffolds with user-defined stiffness. The 3D-printed PGSA-based muscle–tendon scaffolds with tissue-informed material properties support high cell viability and expression of MTJ-related genes such as Itgb1, Tln1, and collagen I. In addition, PGSA-based muscle–tendon constructs also support cellular alignment characteristics of a stable MTJ. Further work in this domain may include the utilization of native human muscle–tendon tissue for mechanical characterization and the utilization of human-derived primary skeletal muscle and tenocytes instead of using mouse cell lines such as C2C12 cells and NIH/3T3 fibroblasts. By utilizing primary human cells, more MTJ-related genes and proteins that are relevant to human muscle–tendon tissue may be investigated to help increase the actual impact of this platform.

Author contributions

Wisarut Kiratitanaporn: conceptualization, methodology, validation, formal analysis, investigation, writing – original draft, writing – review & editing, and visualization. Jiaao Guan: methodology, validation, formal analysis, investigation, writing – review & editing, and resources. Min Tang: methodology, validation, investigation. Yi Xiang: methodology, validation, investigation, and resources. Ting-yu Lu: methodology, validation, investigation, and resources. Alis Balayan: methodology, validation, and investigation. Alison Lao: methodology and resources. David B. Berry: methodology, validation, formal analysis, investigation, writing – review & editing, and resources. Shaochen Chen: conceptualization, supervision, resources, funding acquisition, project administration, writing – original draft, and writing – review & editing.

Data availability

The data supporting the findings in this article are available in the article and in its ESI.† In addition, the derived data supporting the findings in this article are available upon request to the corresponding author.

Conflicts of interest

The authors have no conflict of interest to declare.

Acknowledgements

References

1 Y. Gao and C. Zhang, Structure-function relationship of skeletal muscle provides inspiration for design of new artificial muscle, *Smart Mater. Struct.*, 2015, **24**(3), 033002.

2 R. L. Lieber, *Skeletal muscle structure, function, and plasticity*, Wolters Kluwer Health Adis (ESP), 2011, pp. 1–304.

3 C. Arrigoni, D. Petta, S. Bersini, V. Mironov, C. Candrian and M. Moretti, Engineering complex muscle-tissue interfaces through microfabrication, *Biofabrication*, 2019, **11**(3), 032004.

4 A. B. Knudsen, M. Larsen, A. L. Mackey, M. Hjort, K. K. Hansen, K. Qvortrup, *et al.*, The human myotendinous junction: An ultrastructural and 3D analysis study, *Scand. J. Med. Sci. Sports*, 2015, **25**(1), e116–e123.

5 J. G. Tidball, Myotendinous junction: morphological changes and mechanical failure associated with muscle cell atrophy, *Exp. Mol. Pathol.*, 1984, **40**, 1–12.

6 J. G. Tidball, Force transmission across muscle cell membranes, *J. Biomech.*, 1991, **24**, 43–52.

7 B. R. Eisenberg and R. L. Milton, Muscle fiber termination at the tendon in the frog's sartorius: A stereological study, *Am. J. Anat.*, 1984, **171**(3), 273–284.

8 J. R. Jakobsen and M. R. Krogsgaard, The Myotendinous Junction—A Vulnerable Companion in Sports. A Narrative Review, *Front. Physiol.*, 2021, **12**, 635561, Available from: https://www.frontiersin.org/journals/physiology/articles/10.3389/fphys.2021.635561/full.

9 W. Yaseen, O. Kraft-Sheleg, S. Zaffryar-Eilot, S. Melamed, C. Sun, D. P. Millay, *et al.*, Fibroblast fusion to the muscle fiber regulates myotendinous junction formation, *Nat. Commun.*, 2021, **12**(1), 1–10.

10 C. Alexakis, T. Partridge and G. Bou-Gharios, Implication of the satellite cell in dystrophic muscle fibrosis: A self-perpetuating mechanism of collagen overproduction, *Am. J. Physiol.: Cell Physiol.*, 2007, **293**(2), C661–C669.

11 N. Narayanan and S. Calve, Extracellular matrix at the muscle–tendon interface: functional roles, techniques to explore and implications for regenerative medicine, *Connect. Tissue Res.*, 2021, **62**(1), 53–71.

12 A. Sensini, G. Massafra, C. Gotti, A. Zucchelli and L. Cristofolini, Tissue Engineering for the Insertions of Tendons and Ligaments: An Overview of Electrospun Biomaterials and Structures, *Front. Bioeng. Biotechnol.*, 2021, **9**, 1–23.

13 S. M. McDonald, E. K. Augustine, Q. Lanners, C. Rudin, L. Catherine Brinson and M. L. Becker, Applied machine learning as a driver for polymeric biomaterials design, *Nat. Commun.*, 2023, **14**(1), 4838.

14 S. Calve, K. R. Jacobson, S. Lipp, A. Acuna, Y. Leng and Y. Bu, Comparative analysis of the extracellular matrix proteome across the myotendinous junction, *J. Proteome Res.*, 2020, **19**(10), 3955–3967.

15 V. Burgio, M. Civera, M. Rodriguez Reinoso, E. Pizzolante, S. Prezioso, A. Bertuglia, *et al.*, Mechanical Properties of Animal Tendons: A Review and Comparative Study for the Identification of the Most Suitable Human Tendon Surrogates, *Processes*, 2022, **10**(3), 485.

16 S. Bohm, F. Mersmann and A. Arampatzis, Human tendon adaptation in response to mechanical loading: a systematic review and meta-analysis of exercise intervention studies on healthy adults, *Sports Med. – Open*, 2015, **1**(1), 7.

17 T. K. Merceron, M. Burt, Y. J. Seol, H. W. Kang, S. J. Lee, J. J. Yoo, *et al.*, A 3D bioprinted complex structure for engineering the muscle-tendon unit, *Biofabrication*, 2015, **7**(3), 035003.

18 S. Laternser, H. Keller, O. Leupin, M. Rausch, U. Graf-Hausner and M. Rimann, A Novel Microplate 3D Bioprinting Platform for the Engineering of Muscle and Tendon Tissues, *SLAS Technol.*, 2018, **23**(6), 599–613.

19 M. Josvai, E. Polyak, M. Kalluri, S. Robertson, W. C. Crone and M. Suzuki, An engineered in vitro model of the human myotendinous junction, *Acta Biomater.*, 2024, **180**, 279–294.

20 W. Zhu, X. Qu, J. Zhu, X. Ma, S. Patel, J. Liu, *et al.*, Direct 3D bioprinting of prevascularized tissue constructs with complex microarchitecture, *Biomaterials*, 2017, **124**, 106–115.

21 C. Yu, X. Ma, W. Zhu, P. Wang, K. L. Miller, J. Stupin, *et al.*, Scanningless and continuous 3D bioprinting of human tissues with decellularized extracellular matrix, *Biomaterials*, 2019, **194**, 1–13.

22 X. Ma, X. Qu, W. Zhu, Y. S. Li, S. Yuan, H. Zhang, *et al.*, Deterministically patterned biomimetic human iPSC-derived hepatic model via rapid 3D bioprinting, *Proc. Natl. Acad. Sci. U. S. A.*, 2016, 201524510.

23 X. Ma, C. Yu, P. Wang, W. Xu, X. Wan, C. S. E. Lai, *et al.*, Rapid 3D bioprinting of decellularized extracellular matrix with regionally varied mechanical properties and biomimetic microarchitecture, *Biomaterials*, 2018, **185**, 310–321.

24 J. Koffler, W. Zhu, X. Qu, O. Platoshyn, J. N. Dulin, J. Brock, *et al.*, Biomimetic 3D-printed scaffolds for spinal cord injury repair, *Nat. Med.*, 2019, **25**, 263–269.

25 P. Wang, D. B. Berry, Z. Song, W. Kiratitanaporn, J. Schimelman, A. Moran, *et al.*, 3D Printing of a Biocompatible Double Network Elastomer with Digital Control of Mechanical Properties, *Adv. Funct. Mater.*, 2020, **30**(14), 1–9.

26 J. Ren, P. Han, X. Ma, E. N. Farah, J. Bloomekatz, X. X. I. Zeng, *et al.*, Canonical Wnt5b Signaling Directs Outlying Nkx2.5+ Mesoderm into Pacemaker Cardiomyocytes, *Dev. Cell*, 2019, **50**(6), 729–743.

27 J. Liu, J. He, J. Liu, X. Ma, Q. Chen, N. Lawrence, *et al.*, Rapid 3D bioprinting of in vitro cardiac tissue models using human embryonic stem cell-derived cardiomyocytes, *Bioprinting*, 2019, 1–6.

28 D. B. Berry, S. You, J. Warner, L. R. Frank, S. Chen and S. R. Ward, A 3D Tissue-Printing Approach for Validation of Diffusion Tensor Imaging in Skeletal Muscle, *Tissue Eng., Part A*, 2017, **23**(17–18), 980–988.

29 P. Wang, D. Berry, A. Moran, F. He, T. Tam, L. Chen, *et al.*, Controlled Growth Factor Release in 3D-Printed Hydrogels, *Adv. Healthcare Mater.*, 2019, **9**, 1900977.

30 S. H. Pyo, P. Wang, H. H. Hwang, W. Zhu, J. Warner and S. Chen, Continuous optical 3D printing of green aliphatic polyurethanes, *ACS Appl. Mater. Interfaces*, 2017, **9**(1), 836–844.

31 W. Kiratitanaporn, D. B. Berry, A. Mudla, T. Fried, A. Lao, C. Yu, *et al.*, 3D printing a biocompatible elastomer for modeling muscle regeneration after volumetric muscle loss, *Biomater. Adv.*, 2022, **142**, 213171.

32 R. L. Lieber, *Skeletal muscle structure, function, and plasticity*, Wolters Kluwer Health Adis (ESP), 2011, pp. 1–304.

33 C. L. E. Nijst, J. P. Bruggeman, J. M. Karp, L. Ferreira, A. Zumbuehl, C. J. Bettinger, *et al.*, Synthesis and characterization of photocurable elastomers from poly (glycerol-co-sebacate), *Biomacromolecules*, 2007, **8**, 3067–3073.

34 Y. L. Wu, A. R. D'Amato, A. M. Yan, R. Q. Wang, X. Ding and Y. Wang, Three-Dimensional Printing of Poly(glycerol sebacate) Acrylate Scaffolds via Digital Light Processing, *ACS Appl. Bio Mater.*, 2020, **3**(11), 7575–7588.

35 W. Kiratitanaporn, J. Guan, D. B. Berry, A. Lao and S. Chen, Multimodal Three-Dimensional Printing for Micro-Modulation of Scaffold Stiffness Through Machine Learning, *Tissue Eng., Part A*, 2024, 280–292.

36 S. V. Kontomaris and A. Malamou, Hertz model or Oliver & Pharr analysis? Tutorial regarding AFM nanoindentation experiments on biological samples, *Mater. Res. Express*, 2020, **7**(3), 033001.

37 D. Singh, A. J. Harding, E. Albadawi, F. M. Boissonade, J. W. Haycock and F. Claeyssens, Additive manufactured biodegradable poly(glycerol sebacate methacrylate) nerve guidance conduits, *Acta Biomater.*, 2018, **78**, 48–63.

38 A. Marsano, R. Maidhof, L. Q. Wan, Y. Wang, J. Gao, N. Tandon, *et al.*, Scaffold stiffness affects the contractile function of three-dimensional engineered cardiac constructs, *Biotechnol. Prog.*, 2010, **26**(5), 1382–1390.

39 I. V. Ogneva, D. V. Lebedev and B. S. Shenkman, Transversal stiffness and young's modulus of single fibers from rat soleus muscle probed by atomic force microscopy, *Biophys. J.*, 2010, **98**(3), 418–424.

40 L. E. Bilston and K. Tan, Measurement of Passive Skeletal Muscle Mechanical Properties In Vivo: Recent Progress, Clinical Applications, and Remaining Challenges, *Ann. Biomed. Eng.*, 2015, **43**(2), 261–273.

41 A. H. Lee and D. M. Elliott, Comparative multi-scale hierarchical structure of the tail, plantaris, and Achilles tendons in the rat, *J. Anat.*, 2019, **234**(2), 252–262.

42 G. Lacraz, A. J. Rouleau, V. Couture, T. Söllrald, G. Drouin, N. Veillette, *et al.*, Increased stiffness in aged skeletal muscle impairs muscle progenitor cell proliferative activity, *PLoS One*, 2015, **10**(8), 1–13.

43 D. M. Ebenstein and L. A. Pruitt, Nanoindentation of biological materials, *Nano Today*, 2006, **1**(3), 26–33.

44 J. L. Cuy, A. B. Mann, K. J. Livi, M. F. Teaford and T. P. Weihs, Nanoindentation mapping of the mechanical properties of human molar tooth enamel, *Arch. Oral Biol.*, 2002, **47**(4), 281–291.

45 M. L. Oyen, Nanoindentation of biological and biomimetic materials, *Exp. Tech.*, 2013, **37**(1), 73–87.

46 J. Hay, P. Agee and E. Herbert, Continuous stiffness measurement during instrumented indentation testing, *Exp. Tech.*, 2010, **34**(3), 86–94.

47 R. F. Cook, Probing the nanoscale, *Science*, 2010, **328**(5975), 183–184.

48 P. Rørth, Whence Directionality: Guidance Mechanisms in Solitary and Collective Cell Migration, *Dev. Cell*, 2011, **20**(1), 9–18.

49 C. S. Chen, M. Mrksich, S. Huang, G. M. Whitesides and D. E. Ingber, Geometric control of cell life and death, *Science*, 1997, **276**(5317), 1425–1428.

50 L. Altomare, N. Gadegaard, L. Visai, M. C. Tanzi and S. Farè, Biodegradable microgrooved polymeric surfaces obtained by photolithography for skeletal muscle cell orientation and myotube development, *Acta Biomater.*, 2010, **6**(6), 1948–1957.

51 M. Nikkhah, F. Edalat, S. Manoucheri and A. Khademhosseini, Engineering microscale topographies to control the cell-substrate interface, *Biomaterials*, 2012, **33**(21), 5230–5246.

52 S. H. Pyo, P. Wang, H. H. Hwang, W. Zhu, J. Warner and S. Chen, Continuous optical 3D printing of green aliphatic polyurethanes, *ACS Appl. Mater. Interfaces*, 2017, **9**(1), 836–844.

53 B. N. Allen, R. J. Wendland, J. D. Thompson, B. A. Tucker and K. S. Worthington, Photopolymerization Parameters Influence Mechanical, Microstructural, and Cell Loading Properties of Rapidly Fabricated Cell Scaffolds, *ACS Biomater. Sci. Eng.*, 2023, **9**(5), 2663–2671.

54 K. S. Lim, J. H. Galarraga, X. Cui, G. C. J. Lindberg, J. A. Burdick and T. B. F. Woodfield, Fundamentals and Applications of Photo-Cross-Linking in Bioprinting, *Chem. Rev.*, 2020, **120**(19), 10662–10694.

55 C. D. O'Connell, B. Zhang, C. Onofrillo, S. Duchi, R. Blanchard, A. Quigley, *et al.*, Tailoring the mechanical properties of gelatin methacryloyl hydrogels through manipulation of the photocrosslinking conditions, *Soft Matter*, 2018, **14**(11), 2142–2151.

56 C. Decker, Kinetic study and new applications of UV radiation curing, *Macromol. Rapid Commun.*, 2002, **23**(18), 1067–1093.

57 Z. Z. Bao, M. Lakonishok, S. Kaufman and A. F. Horwitz, α7β1 integrin is a component of the myotendinous junction on skeletal muscle, *J. Cell Sci.*, 1993, **106**(2), 579–589.

58 M. D. Boppart and Z. S. Mahmassani, Integrin signaling: Linking mechanical stimulation to skeletal muscle hypertrophy, *Am. J. Physiol.: Cell Physiol.*, 2019, **317**(4), C629–C641.

59 U. Mayer, Integrins: Redundant or important players in skeletal muscle?, *J. Biol. Chem.*, 2003, **278**(17), 14587–14590.

60 M. R. Buckley, E. B. Evans, P. E. Matuszewski, Y. L. Chen, L. N. Satchel, D. M. Elliott, *et al.*, Distributions of types I, II and III collagen by region in the human supraspinatus tendon, *Connect. Tissue Res.*, 2013, **54**(6), 374–379, DOI: 10.3109/030082072013847096.

61 A. M. Rahimi, M. Cai and S. Hoyer-Fender, Heterogeneity of the NIH3T3 Fibroblast Cell Line, *Cells*, 2022, **11**(17), 2677.

62 F. J. Conti, S. J. Monkley, M. R. Wood, D. R. Critchley and U. Müller, Talin 1 and 2 are required for myoblast fusion, sarcomere assembly and the maintenance of myotendinous junctions, *Development*, 2009, **136**(21), 3597–3606.